Title

Diffusion-to-Imbibition Transition in Water Sorption in Nanoporous Media: Theoretical Studies

Journal

Water Resources Research, 57(6)

ISSN

0043-1397

Authors

Cihan, Abdullah
Tokunaga, Tetsu K
Birkholzer, Jens T

Publication Date

2021-06-01

DOI

10.1029/2021wr029720

Peer reviewed

Diffusion-to-Imbibition Transition in Water Sorption in Nanoporous Media: Theoretical studies

Abdullah Cihan[1], Tetsu K. Tokunaga[1], Jens T. Birkholzer[1]

[1]Energy Geosciences Division, Lawrence Berkeley National Laboratory, USA

Corresponding author: Abdullah Cihan (acihan@lbl.gov)

Key Points:

- The square gradient theory-based model explains diffusion-to-imbibition transition at a critical relative humidity in nanoporous media
- The model presented has an inherent feature to represent hysteresis in adsorption and desorption isotherms.
- Hysteresis in the predicted isotherms is explained by the existence of the different energy barriers for adsorption and desorption.

Abstract

The ability to predict multiphase fluid transport in nanoporous rocks such as shales is critical for many geoscience applications, for example unconventional hydrocarbon production, geologic carbon sequestration, and nuclear waste disposal. When the pore sizes approach nanoscales, the impact of the molecular interaction forces between fluids and solids becomes increasingly important. These forces can alter macroscopic fluid phase behavior and control transport. Recent experimental studies have shown that capillary condensation and subsequent imbibition of liquid water can occur in hydrophilic nanoporous media even if the vapor phase is at a critical relative humidity (rh_{crit}) well below vapor saturation. This study presents a theoretical investigation of the processes controlling adsorption, capillary condensation and imbibition in nanoporous media, using the square-gradient classical density functional theory. The proposed theoretical model explicitly includes the relevant interaction forces among fluids and solids in macroscopic porous media. Application of the model to a relative-humidity-controlled water adsorption experiment is presented to demonstrate the impact of water-pore wall attractive forces on multiphase water behavior in a hydrophilic silicon nanoporous medium. The model represents well the measured time-dependent evolution of the water imbibition front inside the nanoporous medium and also explains the diffusion-like water transport regimes observed at $rh < rh_{crit}$ and the imbibition-like flow regimes observed at $rh > rh_{crit}$. The study furthermore gives an insight on hysteresis phenomenon in adsorption and desorption isotherms.

1 Introduction

The ability to predict multiphase fluid transport in nanoporous rocks is critical for many geoscience applications. For instance, in applications such as geologic carbon sequestration, and nuclear waste disposal (Altman et al., 2014; Zheng et al., 2008), the long-term performance of the selected sites depends on the multiphase physical and chemical interactions in nanoporous caprock or clay-based barriers. Similarly, finding effective strategies for sustainable hydrocarbon production from shale requires understanding of multiphase processes in the nanoporous shale matrix (Alexander et al., 2011; Falk et al., 2015; Tokunaga et al., 2017). When pore sizes approach nanoscales, the impact of molecular interaction forces between fluids and solids becomes increasingly important. The fluid-solid interaction forces, also known as surface forces (e.g., van der Waals, electrostatic, structural forces) (Churaev, 2000; Israelachvili, 2011), result from

electrostatic and electromagnetic fields generated by charges and oscillating molecular dipoles. These forces can alter macroscopic fluid phase behavior and control related processes such as sorption, wetting and transport (e.g., Li et al., 2012; Zarzcyki & Gilbert, 2016; Velasco et al., 2017; Zhang et al., 2017; Berthonneau et al., 2018); they can also cause microstructural changes, especially in clay-rich systems (e.g., swelling, shrinking and fracturing) (e.g., Dehghanpour et al., 2012; Bertoncello, 2014).

Recent experimental research has demonstrated the importance of fluid-solid interfacial interactions on multiphase fluid behavior in nanoporous media, including in shale (e.g., Vincent et al., 2017; Seeman et al., 2017; Zhong et al., 2018; Tokunaga et al., 2017; Cihan et al., 2019; Chakroborty et al., 2020). We recently conducted water transport experiments in shale cores under different relative humidity (rh) conditions and found that the water uptake was significantly greater at rh=0.8 compared to that at rh=0.3 (Tokunaga et al., 2017; Cihan et al., 2019). The experimental finding indicated an enhanced condensation of water at the higher rh. The experiments did not include any measurements of the water concentration inside the sample. However, a macroscopic model, based on the classical density functional theory and fitted to the water uptake measurements suggested that at rh=0.8, the enhanced condensation occurred near the inlet of the core and liquid like water migrated from there to the deeper parts of the core. According to the model results in Cihan et al. (2019), water concentration profiles within the core for rh=0.8 and rh=0.3 differ strongly. In the latter case, the simulated water concentration profiles have a diffusion-type shape and are much smoother than for rh=0.8, where an imbibition-type behavior is predicted.

Previously, Vincent et al. (2017) observed similar phenomena experimentally in a silicon nanoporous system. When they exposed a hydrophilic silicon sample with pore diameters in the 3–4 nm range to water vapor at sufficiently high rh, liquid water condensed near the inlet, and the dense water subsequently filled the nanopores in an imbibition-like manner. Figure 1 shows a schematic diagram that represents the observation of imbibition induced by adsorption and condensation of water under high rh conditions. Vincent et al. (2017) also reported that the transition from smooth diffusion-type concentration profiles to sharp imbibition-type profiles occurred at a threshold value of rh ≈ 0.6. The experiments presented in Vincent et al. (2017) were conducted at 15 ˚C, and it is worth noting that based on the Kelvin equation, capillary condensation in 4 nm pores occurs at rh = 0.58. We believe that this apparent enhanced adsorption and condensation-induced imbibition at well below vapor saturation value is a result of molecular

interactions between water and solid in nanoscale pores which cause phase transition of water vapor, first to adsorbed films and then to pore-filling liquid water. Previous molecular simulation studies based on molecular dynamics, grand canonical Monte Carlo method and classical density functional theory showed that nanoconfinement might influence the phase behavior of fluids (e.g., Peterson & Gubbins, 1987; Evans, 1990; Kierlik et al., 1995; Monson, 2012). However, how the microscopic phenomena affect the macroscopic observation of transitioning from a diffusion-type transport regime to an imbibition-type flow regime is not well understood. Exploring the basic mechanisms controlling adsorption and condensation is important because the underlying fluid-fluid and fluid-solid interaction forces also control flow of multiphase fluids in subsurface nanoporous media.

This paper presents a theoretical model based on the classical density functional theory (cDFT) to provide an understanding of the transition from a diffusion-type transport regime to an imbibition-type flow regime in water sorption in nanoporous media. The model defined in the next section, based on a description of a free energy, includes energy contributions for intermolecular forces between water molecules as well as between water and solid molecules in the nanoporous domain. In Section 3, we qualitatively demonstrate applicability of the model to represent the condensation-induced imbibition data provided by Vincent et al. (2017), which contain optical measurements of water concentration profile changes during water adsorption in a thin silicon nanoporous sample (~1cm×1cm×5μm). The relatively simple pore structure and homogeneous mineral content, compared to natural nanoporous media such as shale, makes Vincent et al. (2017)'s experimental setup suitable for modeling and understanding basic mechanisms of the phase transitions. We present the remarkable features of the model to give insights on 1) both diffusion-type transport regimes at low rh and imbibition-type flow regimes at higher rh, and 2) hysteretic adsorption- desorption isotherms.

2 Methods

2.1 Modeling Approach Based on the Square Gradient Density Functional Theory

The modeling approach presented here is mainly based on Cihan et al. (2019). The important difference in the model presented below is improved descriptions of water phase behavior and surface tension, compared to our earlier model. We first summarize the development of general chemical potential and Darcy-scale momentum equations for an *N*-component fluid

mixture and then present a specific model to describe the transport of liquid and vapor water. The Helmholtz free energy of an inhomogeneous system E_H at a constant temperature can be expressed as

$$E_H = \int_V \psi \, dV \tag{1}$$

where ψ is the local energy density defined as the free energy per unit volume V of a rigid porous medium. Considering the external potentials including the gravitational potential and the interaction potential of the solids acting on the N-component fluid mixture in a porous medium, the Helmholtz free energy density based on the square-gradient approximation can be expressed as

$$\psi = \phi\psi_0 + \frac{\phi^2}{2}\kappa_{ij}\nabla c_i \cdot \nabla c_j + \phi\rho\varphi_g + \phi c_i \varphi_{s,i} \tag{2}$$

where $\psi_0(c_1,c_2,\ldots,c_N)$ is the homogeneous Helmholtz free energy density, defined in terms of energy per unit volume of void space (J/m^3), that represents the intermolecular interactions of water molecules in liquid or gaseous states. ϕ is porosity, and $c_1,c_2,\ldots, c_N$ are the molar concentrations (mol/m^3) of the components that can be in gas or liquid phase. We employ the Einstein summation convention in this paper, i.e. summation is implied over repeated indexes (i=1,…,N and j=1,…,N). The square-gradient term, the second term on the right-hand side of Eq. (2), represents fluid-fluid interfacial energy between different fluid phases and the coefficients κ_{ij} are known as influence parameters (J.m^5/mol^2) related to the correlation functions for molecular densities (Bongiorno et al., 1976; Yang et al., 1976). For the liquid and vapor system under isothermal conditions, it can be assumed that $\kappa_{ij}=\kappa$. A characterization of the influence factor for two-phase liquid-vapor water will be given in the next section. The last two terms of ψ include the external potential energy functions due to gravitational attraction φ_g (J/kg) and fluid-solid interaction potentials for each component, $\varphi_{s,i}$ (J/mol). ρ is the mixture density (kg) equal to $c_i M_i$ where M_i is the molecular mass of the *ith* component (kg/mol).

The chemical potential, Φ_i (J/mol) for the *ith* component is equal to the variational derivative of E_H with respect of c_i and expressed as

$$\Phi_i = \frac{\partial \psi_0}{\partial c_i} - \nabla \cdot \phi \kappa_{ij} \nabla c_j + M_i \varphi_g + \varphi_{s,i}^*$$

$$\varphi_{s,i}^* = \varphi_{s,i} + c_j \frac{\partial \varphi_{s,j}}{\partial c_i} \tag{3}$$

Neglecting the inertial forces due to extremely low fluid velocities in nanodarcy permeability-porous media (Reynolds number <<1), the momentum equation for the multiphase mixture can be expressed as

$$0 = -\frac{\mu \boldsymbol{q}}{k} - \nabla p - \rho \nabla \varphi_g + \phi c_i \nabla \left(\nabla \cdot \kappa_{ij} \nabla c_j \right) - c_i \nabla \varphi_{s,i}^* \tag{4}$$

where $\boldsymbol{q}$ is the Darcy velocity (m/s), k is the permeability of the porous medium (m^2), μ is the viscosity of the fluid mixture (Pa.s), and p is the fluid pressure (Pa). The first three terms in Eq. (4) resemble the classical Darcy equation for single phase flow. Eq. (4) does not include relative permeability for different phases nor does it utilize a macroscopic capillary pressure-saturation function. Instead, the last two terms in Eq. (4) explicitly account for the effects of multiphase interfacial fluid-fluid and fluid-solid interaction forces. Eq. (4) can also be expressed in terms of Φ_i as

$$\boldsymbol{q} = -\frac{k}{\mu} \left(c_i \nabla \Phi_i \right) \tag{5}$$

where, as before, the summation is implied over repeated index i (i=1,…,N). Cihan et al. (2019) applied this momentum equation and the Maxwell-Stefan diffusion equations together with the continuity equations to predict water adsorption and transport in shale. The applied model considered both water and air molecules, but the sensitivity analyses suggested that the contribution of air transport through diffusion and advection to the adsorption and transport of water may be neglected. This is consistent with the fact that diffusion through 2 nm radius capillaries at 1 atm total pressure is in the Knudsen regime, where nearly all collisions involve walls rather than other molecules. As a result, the governing equations for water sorption problem can be substantially simplified. Ignoring the contribution of air, the momentum equation for water molecules in porous media can be written as

$$\boldsymbol{q} = -\frac{k}{\mu} c \nabla \Phi \tag{6}$$

where c is the molar concentration of water (mol/m^3). The diffusive flux of the water in nanoporous matrix may also be expressed as

$$\boldsymbol{J}_d = -\frac{c D}{RT} \nabla \Phi \tag{7}$$

when D is the effective binary diffusion coefficient of water-air fluid system (m^2/s), T is the temperature (K) and R is the ideal gas constant (J/mol/K). Following Vignes's approach (Vignes, 1966) used in Cihan et al. (2019), the effective molecular diffusion coefficient under the two-phase conditions is estimated by interpolation of the diffusivities in liquid and gas phases as $D = D_{(l)}^{x_w} \times D_{(g)}^{1-x_w}$, where x_w is $c / c_{(l)}$ and $c_{(l)}$ is the saturated bulk molar concentration of liquid water at a given T.

The continuity equation for molar concentration of the water can be expressed by

$$\frac{\partial (\phi c)}{\partial t} + \nabla \cdot \left(\boldsymbol{q} c + \phi \boldsymbol{J}_d \right) = 0 \tag{8}$$

The total flux of water molecules through advective and diffusive transport mechanisms in nanoporous media can be expressed as

$$\boldsymbol{J}_t = \boldsymbol{q} c + \phi \boldsymbol{J}_d = -\left(\frac{k c^2}{\mu} + \frac{D \phi c}{RT} \right) \nabla \Phi \tag{9}$$

As will be shown later, in Eq. (9), the first term in the parenthesis dominates under liquid phase conditions whereas the second term in the parenthesis dominates under vapor transport conditions.

As a result, the following second-order partial differential equations are used to describe water adsorption, condensation and imbibition:

$$\frac{\partial (\phi c)}{\partial t} + \nabla \cdot \left(-\frac{k c^2}{\mu} - \frac{D \phi c}{RT} \right) \nabla \Phi = 0 \tag{10}$$

$$\Phi = \frac{\partial \psi_0}{\partial c} - \nabla \cdot \phi \kappa \nabla c + M_w \varphi_g + \varphi_s + c \frac{\partial \varphi_s}{\partial c} \tag{11}$$

where Φ (J/mol) is the overall chemical potential for the water in the pore spaces. Individual definitions of $\partial\psi_0/\partial c$, κ and φ_s are given in the following sections.

2.1.1 Free Energy and Chemical Potential of the Homogeneous Fluid

In this work, we employ an equation of state to represent the homogeneous Helmholtz free energy and chemical potential of water ($\partial\psi_0/\partial c$). Developing an equation of state for water is challenging and different equations were developed in varying complexity and accuracy. We used an equation of state given by Fuller (1976), presented in Appendix A. Based on the Fuller equation of state, the chemical potential of the homogeneous fluid (Φ_0) were given by Guerrero and Davis (1980) as

$$\frac{\partial\psi_0}{\partial c}=\Phi_0=\psi_0^+(T)+\frac{bcRT}{1-bc}-\frac{ac}{1+bc\chi}-RT\ln\left(\frac{1}{c}-b\right)-\frac{a}{b\chi}\ln(1+cb\chi) \tag{12}$$

where a (J.m^3/mol^2) and b (m^3/mol) are the attraction energy and the excluded volume parameters, respectively. χ is a temperature dependent parameter introduced by Fuller (1976), and in the limit of χ=0 the equation of state given in Appendix A becomes the van der Waals equation and in the limit of χ=1, becomes the Redlich-Kwong-Soave equation. $\psi_0^+(T)$ is the ideal gas contribution to the energy as a function of temperature only and cancels out during the computations under isothermal conditions in this work. The equilibrium liquid, $c_{(l)}$, and vapor, $c_{(v)}$, concentrations of the coexisting phases at a given T are found from solving $p(c_{(l)})=p(c_{(v)})$ and $\Phi_0(c_{(l)})=\Phi_0(c_{(v)})$. As demonstrated in Figure A1, the predicted saturated density of liquid and vapor water are in reasonable agreement with a more accurate but much more complex equation of state Wagner & Pruss, 2002).

The equilibrium concentrations for water can be expected to vary under the influences of water-solid mineral interactions in nanoscale pores. Cihan et al. (2019) proposed an exponential function to describe macroscopically the fluid-solid interaction potential, based on coarse-grained molecular simulation studies in cylindrical nanopores. We describe the water-solid interaction potential using a similar simple expression as

$$\varphi_s=A_h\exp(-c\alpha) \tag{13}$$

where A_h (J/mol) and α (m^3/mol) are empirical parameters that may vary depending on pore geometry, pore sizes, and fluid and solid molecule types. The magnitudes and signs of the parameters may vary depending on wettability of solids. A_h is negative and α is positive for interaction of water with hydrophilic pore walls. Eq. (13) suggests that absolute value of the interaction potential between water and the hydrophilic solid decreases exponentially with increasing concentration of water. An estimation of these parameters for the hydrophilic silicon nanoporous medium will be given in Section 3.

2.1.2 Influence Parameter and Surface Tension

The statistical mechanics definition of the influence parameter (κ) is given in terms of the molecular correlation functions (Bongiorno et al., 1976; Yang et al., 1976). A direct prediction of the influence parameter is possible only for simple fluid systems with known correlation functions. However, the influence parameter can be linked to attraction energy (a) and excluded volume (b) parameters of the equation of state as demonstrated by Carey et al. (1978) and Guerrero & Davis (1980):

$$\kappa(T) = \upsilon(T)\, a\, b^{2/3} \tag{14}$$

The temperature-dependent coefficient υ(T) in Eq. (14) is not universal and changes for different fluids. The surface tension is related to κ multiplied by the magnitude of the concentration square gradient. The definition of the surface tension according to the square gradient theory and the calculation procedure are given in Appendix B. Figure B1 shows an almost perfect fit of the square gradient theory-based model to the surface tension data for water. We estimated that the temperature dependent coefficient for water can be expressed as $\upsilon(T) = \left(0.6058 T_r + 0.0556\right)^2$, where T_r is the ratio of the temperature to the critical temperature. The value of κ at T=15^{o}C is equal to about 9.23×10^{-21} (J.m^5/mol^2). The thickness of the interfacial zone at that temperature is only in the order of a few molecular diameter (Figure B2). Representing such a thin interfacial zone requires a model resolution much smaller than a few molecular diameter (grid size ≈0.012 nm in Appendix B). If the model resolution is decreased while keeping κ constant, the value of the surface tension changes because the concentration gradient changes. As achieving such a high model resolution is prohibitive for a macroscopic modeling study, κ is typically scaled up by the square of the numerical model grid size to compensate for the decreased concentration gradient

with decreasing model resolution so that the magnitude of the surface tension stays approximately same (Cueto-Felgueroso & Juanes, 2018; Cihan et al., 2019). In addition to the model resolution, in macroscopic modeling studies of complex porous media, κ is expected to be a function of pore size distribution and connectivity. However, given the uniformity of pore sizes and the lateral continuity of pores for the nanoporous medium tested in this work, as explained in the next section, we assume κ is only functions of temperature and model resolution. We scale up the κ value by the square of the ratio of the macroscopic model grid size to the molecular model grid size (0.012 nm), as expressed in Table 1, to represent the surface tension energy between the liquid and gas phases.

2.2 Modeling Laboratory Test of Imbibition Triggered by Adsorption and Condensation

In this study, we used the experimental data in Vincent et al. (2017) that established the migration of water in an imbibition like manner during water vapor adsorption, as conceptually represented in Figure 1. Vincent et al. (2017) used a thin silicon nanoporous sample (~1cm×1cm×5μm). The porosity is quite high (~0.45), and the equivalent pore radii were reported to range between 1.5-2 nm. Vincent et al. (2017) does not include a detailed image of actual pore structure in their sample. The imaging studies by Elia et al. (2016), using SEM micrographs, for the similar type silicon nanoporous media (porosity range = 0.34 – 0.47) indicate that the pore structure involves more or less parallel and laterally connected tortuous paths. Homogeneous mineral content and the simple pore structure with roughly uniform pore sizes appear to be consistent with the assumptions behind the expression for the fluid-solid and the fluid-fluid interactions.

The data provided in Vincent et al. (2017) include the measurement of the relative changes in reflectance using an optical approach. The relative changes in grayscale intensity with respect to the intensity at dry state were quantified to track the motion of the water inside the nanoporous sample. Vincent et al. (2017) stated that there would be a close-to-linear relationship between adsorbed mass and reflectance. Vincent et al. (2017) did not report an established correlation to map the measured relative change in reflectance to the actual adsorbed water mass or average water concentration, and thus currently we do not know if the accuracy of ‘the close-to-linear relationship’ is the same for high water saturations and low water saturations. Vincent et al. (2017) reported spurious spikes in reflectance that occurred during desorption and later stages of the

condensation. Despite the qualitative nature of the data collected, the reflectance method of Vincent et al. (2017) showed that the imbibition front in their silicon nanoporous sample could still be reasonably detected. Therefore, we focused here on representing the imbibition front using the model, rather than exactly matching the concentration values.

For our analyses in this work, we digitized Vincent et al. (2017)'s data given for a high relative humidity condition (rh=0.98) and then we expressed the relative change in intensity data in terms of average dimensionless concentrations, by simply taking the ratio of the relative intensities to the relative intensity at fully wet condition (Figure 2). The silicon nanoporous sample was exposed to water vapor at one inlet boundary, while keeping the other boundaries closed. We used the one-dimensional version of the model presented in the previous section without gravitational forces because of infinitesimally small Bond number, for both simulating the experiment in Vincent et al. (2017) and subsequent numerical analyses. The following initial and boundary conditions were employed to solve the equations:

$$\begin{aligned} &c(x,t=0)=0;\ \Phi(x,t=0)=\Phi_0(c_v(0)) \\ &c(x=0,t)=c_v\left(rh\right);\ \Phi(x=0,t)=\Phi_0(c_v(rh)), \qquad \text{(inlet)} \\ &qc(x=L,t)+J_d(x=L,t)=0 \end{aligned} \tag{15}$$

where L is the length of the sample (1 cm). An in-house computer model was employed to numerically solve the coupled second order partial differential equations in Eqs. (10-11) based on the finite volume method. The numerical model domain was finely discretized using a uniform grid size of Δx=12.5 μm. The system of equations is linearized using the Newton-Raphson method and solved simultaneously by a preconditioned restarted Generalized Minimum Residual algorithm.

3 Results and Discussion

The numerical model was fitted to the experimental data using the Differential Evolution optimization algorithm (Price et al., 2005) to estimate the five unknown parameters listed in Table 2. Figure 2 shows the model-estimated concentration profiles and the experimental data at rh=0.98, extracted based on the relative change in reflectance from Vincent et al. (2017). The profiles clearly show imbibition like transport of water inside the nanoporous medium. The model appears to represent the water concentration profiles at different times reasonably well. The estimated permeability appears to be very low, about 9 nanodarcy, but this is about an order of magnitude

greater than what we previously estimated for a Marcellus shale rock core with a porosity of 0.1 in Cihan et al. (2019). The estimated effective diffusion coefficients are also an order of magnitude greater than the estimated values for the same shale and the reported values for other nanoporous rocks (Peng et al., 2012; Zhang et al., 2017; Tokunaga et al., 2017). The ideal Knudsen diffusion coefficient in a cylindrical pore of 2 nm radius is about 8×10^{-7} m^2/s, which is in the same order of magnitude with our estimated diffusivity value for the gas phase, $D_{(g)}= 2.78\times10^{-7}$ m^2/s. Considering that the ideal Knudsen diffusivity must be scaled down to account for the tortuosity, our estimated value of $D_{(g)}$ appears reasonable.

The estimated $D_{(l)}$ is about two orders of magnitude less than the self-diffusion coefficient of water, 1.77×10^{-9} m^2/s at 15 ˚C (Holz et al., 2000). The finding of the reduced water diffusivity is consistent with the experimental measurements in other hydrophilic nanoporous media. For example, the ratio of the self-diffusivity of water to the measured diffusivity in cement paste was found to be in range of 60 to 80 (Li et al., 2012; Korb et al., 2007). The measurements of the reduced self-diffusivity of water in hydrophilic confined pore spaces were also supported by molecular simulation studies (e.g., Kalinichev et al., 2007; Bonnaud et al., 2010; Qomi et al., 2014). The molecular simulation study by Bonnaud et al. (2010) shows that the self-diffusivity decreases with decreasing nanopore size. In general, based on the molecular simulations, the reduced diffusivity is explained by structuring of water molecules near the hydrophilic surfaces and tendency of hydrogen atoms of water to orient and move toward the surfaces, which slows down the movement of water molecules. As a result, the diffusivity of water in nanoporous media may become significantly lower than the diffusivity of bulk water.

In this work, $D_{(l)}$ does not seem to significantly affect the model results at the early stage of adsorption and condensation. However, in the later stages of the condensation, because the value of $D_{(l)}$ is orders of magnitude smaller than the value of $D_{(g)}$, the interpolated D, (see Section 2.1), becomes smaller and smaller as the water concentration increases. As a result, in the imbibition like water transport regime, the total diffusive term becomes much smaller compared to the advective term.

Based on Eq. (9) with the estimated permeability and the diffusivities, Figure 3 shows that the contribution to the total water flux is dominated by the diffusive term when the normalized water concentration (or saturation) stays low, which can occur, as demonstrated below, at low rh

conditions. At high rh conditions where the normalized water concentration substantially increases as a result of the phase transitions to pore-filling liquids in the 2 nm radii pores, the total flux is largely due to the advective term.

3.1 Diffusion-to-Imbibition Transition

Consistent with the experimental finding reported in Vincent et al. (2017), the model results show that there exists a critical rh value (rh_{crit}) equal to 0.6. When rh < rh_{crit}, smooth, diffusion-type concentration profiles occur, and when rh > rh_{crit}, sharp and imbibition-type concentration profiles appears (e.g., Figures 4a and 4b). The diffusion-type profiles calculated for rh=0.5 in Figure 4a indicates that water migrates mainly with vapor diffusion and forms adsorbed films in the pores. In Figure 4b, the model calculations at early times show smooth concentration profiles as water vapor diffuses and becomes adsorbed in the pores. At later times, with the sufficient supply of water molecules under high rh conditions (0.8 in this case), the diffusion-type profiles transition into the imbibition-type profiles. The transition from adsorbed water film to pore filling liquid starts at near the inlet, and then the water migrates in an imbibition-like fashion. When rh < rh_{crit}, this transition does not happen and the normalized water concentration (or saturation) remains low. According to the model, the transition time for diffusion-to-imbibition depends on rh. Figure 5 shows a plot of the rh-dependence of the model-calculated elapsed times when the transition occurs at a short distance from the inlet (x≈0.68 mm). As the rh increases, the chemical potential difference between the outside and the inside of the porous medium increases, and the transition to imbibition develops more rapidly. As the rh approaches the rh_{crit}, the transition requires much longer time, consistent with time needed to diffusively build up adsorbed film thicknesses to the point of pore filling.

3.2 Equilibrium Behavior of Water and Adsorption-Desorption Isotherms in the Silicon Nanoporous Medium

The occurrence of the diffusion-to-imbibition transition at high rh (>rh_{crit}) can be understood by evaluating the thermodynamic potential of the system. We employ a useful thermodynamic potential known as the grand potential, (Evans, 1990),

$$\Omega = \psi_0 + c\varphi_s - c\Phi_0\left(c_v\right) \tag{16}$$

where Ω represents the grand potential density (J/m^3). Eq. (16) can be used to explain the equilibrium properties of water (i.e., the adsorbed films or pore filling condensed water) inside the nanoporous medium that is in equilibrium with water vapor (c_v) kept at different fixed rh values and chemical potentials ($\Phi_0(c_v)$).

Figure 6a shows a plot of the grand potential energy density as a function of the normalized water concentration for the nanoporous medium tested at various rh conditions. At rh < 0.6, the grand potential function shows two local minima. The minima in the potential correspond to possible stable equilibrium concentrations of water in the pore space when the equilibrium is reached. During water adsorption for rh <0.6, starting from a dry state, water concentration increases and the potential reaches the first minimum where the stable adsorbed films form. There exists an energy barrier preventing the adsorbed films from growing into pore-filling condensed liquid phase. Note that there is no any initial barrier to create adsorbed films (i.e., very left side of the curves, left to the first minimum), because the water-solid attractive forces are strong and sufficient for creation of adsorbed surface layers (~mono- or few-molecular thicknesses). However, at low rh values, the water-solid attractive potential is not enough to form liquid bridges across the entire pores. As a result, during adsorption at rh < rh_{crit}=0.6, the system reaches an equilibrium with a lower water concentration, corresponding to the first minimum of the potential function. The energy barrier decreases with increasing relative humidity and finally disappears at the critical relative humidity of 0.6 for water in the silicon nanoporous medium. When rh > rh_{crit}=0.6, we do not see any stable adsorbed films, and instead the potential energy reaches a minimum with a high water concentration by taking up much more water from the outside. As a result, imbibition-type water transport regime results when rh > rh_{crit}=0.6.

Figure 6b presents a conceptual energy diagram based on Eq. (16) to explain the phase transitions. The diagram represents the free energy changes at different rh conditions (> or < rh_{crit}). When the fluid-solid interaction is zero, i.e., the top curve, the grand potential show two local minima corresponding to the bulk saturated liquid and vapor concentrations, as would be calculated from the equation of state. Figure 6b shows that in addition to the energy barrier for adsorption, there exists an energy barrier for desorption. For desorption, additional energy is needed to overcome the attractive forces between water molecules and between water and solid molecules. The energy associated with these attractive forces represents the second energy barrier

shown in Figure 6b. However, the energy barrier for desorption is much deeper than the energy barrier for adsorption, and this means that a much greater chemical potential difference is needed for desorption of water from pore space than for adsorption of water into pore space.

Figure 7 exhibits an interesting feature of the model to represent hysteresis in adsorption and desorption isotherms at 15^{o}C. The difference in the energy barriers of adsorption and desorption (Figure 6b) appears to be responsible for our model prediction of hysteresis in adsorption-desorption isotherms. Each point in Figure 7 was obtained by solving Eqs. (10-11) until the steady state was reached under different rh boundary conditions. At equilibrium, the chemical potential (Eq. 11) becomes constant throughout the domain. Although the difference in the energy barriers is the reason for the calculated hysteresis of adsorption-desorption isotherms in the idealized porous medium here with the bundle of more or less uniformly sized nanopores, pore connectivity and pore size distributions are the other important factors for the hysteretic isotherms in more complex porous media (e.g., Haines, 1930; Monson, 2012). It should be noted that the model calculated isotherms in Figure 7 appear to be very sharp, especially compared to the reflectance isotherms presented in Vincent et al. (2017) for T=15^{o}C. Sharpness or slope of the isotherms presumably reflects how the pore sizes vary in the nanoporous medium. We do not know exactly how the reflectance values are related quantitatively to the total adsorbed mass of the water in the silicon nanoporous medium, but small changes in the pore sizes may cause variation of the phase behavior (adsorbed film versus pore filling) in individual pores, and this can in turn make the isotherms representing the overall behavior of the pore network smoother. The fact that the model calculated isotherms look very sharp implies that the current representation of the impacts of the fluid-solid interaction forces in the model needs to be improved to represent the adsorption-desorption isotherms in porous media with broad pore size distributions.

4 Conclusions

This study presents a theoretical investigation of the processes controlling adsorption, capillary condensation and imbibition in a nanoporous medium. The theoretical model, which is based on the square-gradient density functional theory, explicitly includes the relevant interaction forces among fluids and solids in macroscopic nanoporous media. We applied the model to a relative humidity-controlled water adsorption experiment in a hydrophilic silicon nanoporous medium by Vincent et al. (2017). The model represents reasonably well the data for the time-

dependent evolution of the water imbibition front inside the nanoporous medium that was observed under a high rh boundary condition. The model also correctly represents the critical relative humidity value (rh_{crit}) of 0.6 for the transition to happen from diffusion-type transport regime to an imbibition-type transport regime of water. The model shows that when rh exceeds rh_{crit}, smooth and diffusion-type concentration profiles change into sharp and imbibition-type concentration profiles (Figures 4a and 4b). The model results indicate that the transition from adsorbed water film to pore filling liquid starts near the inlet, and then the water migrates in an imbibition-like fashion into deeper parts of the core. We found that for $rh > rh_{crit}$, the transition time substantially increases as rh decreases towards rh_{crit}. This is because the chemical potential difference between the outside and the inside of the porous medium decreases with decreasing rh. Remarkably, the model presented has an inherent feature to predict hysteresis in adsorption and desorption isotherms. We presented an explanation for the occurrence of hysteresis using the grand potential formulated based on the model and showed that the different energy barriers for adsorption and desorption lead to hysteresis in adsorption-desorption isotherms. However, our analyses show that the free energy description in the model that includes the fluid-solid interaction forces will need to be improved for more accurately representing the adsorption-desorption isotherms in natural nanoporous media with broad pore size distributions.

Acknowledgments

This material is based on work supported by U.S. Department of Energy (DOE), Chemical Sciences, Geosciences, and Biosciences Division and Office of Fossil Energy, Office of Natural Gas and Petroleum Technology under Contract DE-AC02-05CH11231. All data from this study is available at https://doi.org/10.5281/zenodo.4480378. The source code for this research is not currently publicly posted due to the intellectual property transfer policy in our institution but is available upon request from the corresponding author and approval from the Intellectual Property Office (IPO@lbl.gov) of Lawrence Berkeley National Laboratory.

Appendix A: Equation of State for Water

Fuller's equation of state (1976) for water in terms of pressure (P) as a function of molar concentration of water (c) and temperature (T) is expressed as

$$P = \frac{cRT}{1-cb} - \frac{c^2 a}{1+cb\chi} \tag{A1}$$

where a is the attraction energy parameter (J.m^3/mol^2), b is the excluded volume parameter (m^3/mol), and χ is a temperature dependent dimensionless parameter introduced by Fuller (1976):

$$a = \Omega_a(\beta)\frac{R^2 T_c^2 \alpha(T_r)}{P_c},\ b = \Omega_b(\beta)\frac{RT_c}{P_c},\ \chi = \frac{1}{\beta}\left(\sqrt{\frac{1}{\beta}-\frac{3}{4}}-\frac{3}{2}\right) \tag{A2}$$

The formulations of other parameters are presented as

$$\begin{aligned}
&\beta_c = c_c b \\
&Z_c(\beta) = \frac{P_c v_c}{RT_c} = \frac{(1-\beta_c)(2+\chi_c\beta_c)-(1+\chi_c\beta_c)}{(2+\chi_c\beta_c)(1-\beta_c)^2} \\
&\beta_0 = \beta_c\left(7.788 - 36.8316 Z_c + 50.7061 Z_c^2\right) \\
&\theta = 10.9356 + 0.0285\overline{P} \\
&\beta = \beta_c + (\beta_0 - \beta_c)\left[\frac{2}{1+\mathrm{e}^{\theta(T_r-1)}} - 1\right] \\
&\Omega_b(\beta) = \beta\frac{(1-\beta)(2+\chi\beta)-(1+\chi\beta)}{(2+\chi\beta)(1-\beta)^2} \\
&\Omega_a(\beta) = \frac{(1+\chi\beta)^2\Omega_b(\beta)}{\beta(2+\chi\beta)(1-\beta)^2} \\
&q(\beta) = \left(\frac{\beta}{0.26}\right)^{1/4}(0.480 + 1.574\omega_a - 0.176\omega_a^2) \\
&\alpha(T_r) = [1+q(\beta)(1-T_r^{1/2})]^2
\end{aligned} \tag{A3}$$

where T_r is the reduced temperature, T/T_c. The specific parameter values for water that is necessary for computing the equation is given as $\overline{P} = 54.2,\ T_c = 647.3K,$ $P_c = 2.205\times10^7\ Pa,\ c_c = 17900\,\mathrm{mol/m^3},\ Z_c = 0.229,\ \omega_a = 0.344$.

Based on the Fuller equation of state, the Helmholtz free energy density of the homogeneous fluid is expressed by (Guerrero & Davis, 1980),

$$\psi_0(c) = c\psi_0^+(T) - cRT\left[\ln(1/c-b)+1\right] - \frac{ca}{b\chi}\ln(1+cb\chi) \tag{A4}$$

where $\psi_0^+(T)$ is the ideal gas contribution and cancels out during the computations in this work. The equilibrium liquid, $c_{(l)}$, and vapor, $c_{(v)}$, concentrations of the coexisting phases at a given T are found by solving two algebraic equations simultaneously $p(c_{(l)}) = p(c_{(v)})$ and $\Phi_0(c_{(l)}) = \Phi_0(c_{(v)})$. Figure A1 shows that the predicted saturated density of liquid and vapor water are in reasonable agreement with the results based on the IAPWS formulation for water (Wagner and Pruss, 2002) at different temperatures. The mean difference between the calculated saturated liquid density values is about 2.5 %, and the mean difference for the calculated saturated vapor density values is about 10 %. However, at 15 ^{o}C, the difference between the liquid densities is less than 1%, while the difference between the vapor densities increase to 24 %.

Appendix B: Square Gradient Theory of Surface Tension

For a planar liquid and vapor interface in a non-porous medium, the equilibrium concentration distribution, according to the square gradient theory, can be described by the following second order partial differential equation and fixed concentration boundary conditions:

$$\Phi = \frac{\partial \psi_0(c,T)}{\partial c} - \kappa(T)\frac{d^2c}{dx^2},\ c\left(x \to \infty\right) = c_v,\quad c\left(x \to -\infty\right) = c_l \tag{B1}$$

The surface tension coefficient is described as

$$\gamma = \int_{-\infty}^{\infty} \kappa\left(\frac{\partial c}{\partial x}\right)^2 dx \tag{B2}$$

By manipulation of Eq. (B1), Eq. (B2) can be expressed as functions of the saturated liquid and vapor concentrations only (Teletzke et al., 1982):

$$\gamma = \sqrt{2}\int_{c_v}^{c_l} \sqrt{\kappa(\Omega - \Omega_v)}\, dc \tag{B3}$$

where

$$\begin{aligned} \Omega &= \psi_0(c) - c\,\Phi_0\left(c_v\right) \\ \Omega_v &= \psi_0(c_v) - c_v\,\Phi_0\left(c_v\right) \end{aligned} \tag{B4}$$

and Φ_0 is the chemical potential of the homogeneous fluid as given by Eq. (12), and the equilibrium liquid, c_l, and vapor, c_v, concentrations of the coexisting phases at a given *T* are calculated as described in Appendix A. The temperature dependent coefficient υ(T) in the influence parameter, κ, in Eq. (14) is estimated by fitting Eq. (B3) to the surface tension data for water (Figure B1). Note that Eq. (B3) was evaluated by numerical integration, and we found that the temperature dependent coefficient for water can be expressed as $\upsilon(T) = (0.6058T_r + 0.0556)^2$. With the knowledge of the equation of state and the influence parameter, we numerically solved Eq. (B1) using the Finite Volume method as described in Section 2 at different grid resolutions. Then we computed the concentration profiles (Figure B2) and the surface tension from Eq. (B2). By comparing the numerical results against the data, we found that a grid size of about 0.012 nm would produce surface tension values accurate up to fourth digit. As a result, we selected this grid size as a base to scale up the influence parameter for macroscopic simulations at a micrometer-scale model resolution, as described in Section 2.1.2.

References

Alexander, T., Baihly, J., Boyer, C., Clark, B., Waters, G., Jochen, V., Calvez, J. Le, Lewis, R., Miller, C. K., Thaeler, J., & Toelle, B. E. (2011). Shale gas revolution. *Oilfield Review*, 23, 40–55.

Altman, S. J., Aminzadeh, B., Balhoff, M. T., Bennett, P. C., Bryant, S. L., Cardenas, M. B., Chaudhary, K. et al. (2014). Chemical and hydrodynamic mechanisms for long-term geological storage. *J. Phys. Chem. C*, 118, 15103-15113.

Berthonneau, J., Obliger, A., Valdenaire, P.L., Grauby, O., Ferry, D., Chaudanson, D., Levitz, P., Kim, J. J., Ulm, F.J., & Pellenq, R. J. (2018). Mesoscale structure, mechanics, and transport properties of source rocks' organic pore networks. *Proceedings of the National Academy of Sciences*, 115 (49), 12365-12370.

Bertoncello, A., Wallace, J., Blyton, C., Honarpour, M., & Kabir, C. S. (2014). Imbibition and water blockage in unconventional reservoirs: Well-management implications during flow back and early production. *SPE Reservoir Evaluation & Engineering*, 17(4), 497–506.

Bongiorno, V., Scriven, L. E., & Davis, H. T. (1976). Molecular theory of fluid interfaces. *J. Colloid Interface Sci.*, 57, 462.

Bonnaud, P. A., Coasne, B., & Pellenq, R. J-M. (2010). Molecular simulation of water confined in nanoporous silica. *Journal of Physics: Condensed Matter*, 22, 284110.

Carey, B. S., Scriven, L. E., & Davis, H. T. (1978). Semiemprical theory of surface tensions of pure normal alkanes and alcohols. *AIChE Journal*, 24(6).

Chakraborty, N., Karpyn, Z., Liu, S., Yoon, H., & Dewers, T. (2020). Experimental evidence of gas densification and enhanced storage in nanoporous shales. *Journal of Natural Gas Science and Engineering*, *76*, 103120.

Churaev, N. V. (2000). Liquid and vapor flows in porous bodies: surface phenomena, CRC press, New York.

Cihan, A., Tokunaga, T. K., & Birkholzer, J. T. (2019). Adsorption and condensation-induced imbibition in nanoporous media. *Langmuir*, 35 (29), 9611-9621.

Cueto-Felgueroso, L., Fu, X., & Juanes, R. (2018). Pore-scale modeling of phase change in porous media. *Physical Review Fluids*, 3, 084302.

Dehghanpour, H., Zubair, H. A., Chhabra, A., & Ullah, A. (2012). Liquid uptake of organic shales. *Energy Fuels*, 26, 5750-5758.

Elia, P., Nativ-Roth, E., Zeiri, Y., Porat, Z. (2016). Determination of the average pore-size and total porosity in porous silicon layers by image processing of SEM micrographs. *Microporous and Mesoporous Materials*, 225, 465-471.

Evans, R. (1990). Fluids adsorbed in narrow pores: phase equilibria and structure. *Journal of Physics: Condensed Matter, 2*, 8689-9007.

Falk, K., Coasne, B., Pellenq, R., Ulm, F.J, & Bocquet, L. (2015). Subcontinuum mass transport of condensed hydrocarbons in nanoporous media. *Nature Communications*, 6, 6949.

Fuller, G. G. (1976). A modified Redlich-Kwong-Soave equation of state capable of representing the liquid state. *Ind. Eng. Chem. Fundam.*, 4 (15), 254-257.

Guerrero, M. I., & Davis, H. T. (1980). Gradient theory of surface tension of water. *Ind. Eng. Chem. Fundam.*, 19, 309-311.

Haines, W. B. (1930). Studies in the physical properties of soil. V. The hysteresis effect in capillary properties, and the modes of moisture distribution associated therewith. *The Journal of Agricultural Science, 20*(1), 97-116.

Holz, M., Heil, S. R., & Sacco, A. (2000). Temperature-dependent self-diffusion coefficients of water and six selected molecular liquids for calibration in accurate ^{1}H NMR PFD measurements. *Phys. Chem. Chem. Phys.*, 2000, 2, 4740-4742.

International Association for the Properties of Water Steam (1994). IAPWS release on surface tension of heavy water substance. *In Physical Chemistry of Aqueous Systems: Proceedings of the 12th International Conference on the Properties of Water and Stem*, Orlando, FL, 1994, a103-a106.

Israelachvili, J. N. (2011). Intermolecular and Surface Forces. Elsevier, 3rd edition.

Kalinichev, A. G., Wang, J., & Kirkpatrick, R. J. (2007). Molecular dynamics modeling of the structure, dynamics and energetics of mineral – water interfaces: Application to cement materials. *Cement and Concrete Research*, 37, 337 – 347.

Kierlik, E., Fan, Y., Monson, A., & Rosinberg, M. L. (1995). Liquid-liquid equilibrium in a slit pore: Monte Carlo simulation and mean field density functional theory. *J. Chem. Phys.*, 102 (9), 3712.

Korb, J.-P., Monteilhet, L., McDonald, P. J., & Mitchell J. (2007). Microstructure and texture of hydrated cement-based materials: A proton field cycling relaxometry approach. *Cement and Concrete Research*, 37, 295 – 302.

Li, H., Fratini, E., Chiang, W.-S., Baglioni, P., Mamontov, E., & Chen, S.-H. (2012). Dynamic behavior of hydration water in calcium-silicate-hydrate gel: A quasielastic neutron scattering spectroscopy investigation. *Physical Review E*, 86, 061505.

Li, L., Kazoe, Y., Mawatari, K., Sugii, & Y., Kitamori, T. (2012). Viscosity and wetting property of water confined in extended nanospace simultaneously measured from highly-pressurized meniscus motion. *J. Phys. Chem. Lett., 3* (17), 2447–2452.

Monson, P. A. (2012). Understanding adsorption/desorption hysteresis for fluids in mesoporous materials using simple molecular models and classical density functional theory. *Microporous and Mesoporous Materials*, 160, 47-66.

Peng, S., Hu, Q. H., & Hamamoto, S. (2012). Diffusivity of rocks: Gas diffusion measurements and correlation to porosity and pore size distribution. *Water Resources Research*, 48. W02507.

Peterson, B. K. & Gubbins, K. E. (1987). Phase transitions in cylindrical pore. *Molecular Physics*, 62(1), 215-226.Price, K., Storn, R., & Lampinen, J. (2005). Differential evolution: A practical approach to global optimization. Springer, Berlin, Germany.

Qomi, M. J. A., Bauchy, M., Ulm, F.-J., & Pellenq, R. J.-M. (2014). Anomalous composition-dependent dynamics of nanoconfined water in the interlayer of disordered calcium-silicates. *J. Chem. Phys.*, 140, 054515.

Seeman, T., Bertier, P., Krooss, B. M., Stanjek, H. (2017). Water vapor sorption on mudrocks. In Geomechanical and Petrophysical Properties of Mudrocks, edited by E. H. Rutter, et al., 201-233, Geological Society of London, London.

Teletzke, G. F., Scriven, L. E., & Davis, H. T. (1982). Gradient theory of wetting transitions. *Journal of Colloid and Interface Science*, 87(2), 550-571.

Tokunaga, T. K., Shen, W. J., Wan, J. M., Kim, Y., Cihan, A., Zhang, Y. Q., & Finsterle, S. (2017). Water saturation relations and their diffusion-limited equilibration in gas shale: Implications for gas flow in unconventional reservoirs. *Water Resour. Res.*, 53(11), 9757-9770.

Velasco, R., Pathak, M., Panja, P., & Deo, M. (2017). What happens to permeability at the nanoscale? A molecular dynamics simulation study. *Unconventional Resources Technology Conference*, doi:10.15530/URTEC-2017-2697415.

Vignes, A. (1966). Diffusion in binary solutions. *Ind. Engng J.*, 5, 189-199.

Vincent, O., Marguet, B., & Stroock, A. D. (2017). Imbibition triggered by capillary condensation in nanopores. *Langmuir*, 33, 1655−1661.

Wagner, W., & Pruss, A. (2002). The IAPWS formulation 1995 of the thermodynamics properties of ordinary water substance for general and scientific use. *Journal of Physical and Chemical Reference Data* 31, 387; doi: 10.1063/1.1461829.

Yang, A. J. M., Fleming III, P. D., Gibbs, J. H. (1976). Molecular theory of surface tension. *The Journal of Chemical Physics*, 64, 3732.

Zarzycki, P., & Gilbert, B. (2016). Long-Range Interactions Restrict Water Transport in Pyrophyllite Interlayers. *Sci Rep* 6, 25278.

Zhang, Y., Mostaghimi, P., Fogden, A., Middleton, J., Sheppard, A., & Armstrong, R. T. (2017). Local diffusion coefficient measurements in shale using dynamic microcomputed tomography. *Fuel*, 207, 312–322.

Zheng, L., Samper, J., Montenegro, L., & Mayor, J. C. (2008). Multiphase flow and multicomponent reactive transport model of the ventilation experiment in Opalinus clay. *Physics and Chemistry of the Earth*, 33, S186-S195.

Zhong, J., Riordon, J., Zandavi, S. H., Xu, Y., Persad, A. H., Mostowfi, F., & Sinton, D. (2018). Capillary condensation in 8 nm deep channels. *J. Phys. Chem. Lett.*, 9, 497−503.

Table 1. Model input parameters for water in the hydrophilic silicon nanoporous medium (pore radius~2 nm, and T=15^{o}C)

ϕ (-)	0.45
μ_w (Pa.s)	1.14×10^{-3}
$D_{aw\ (l)}$ (m^2/s)	2.25×10^{-9}
$D_{aw\ (g)}$ (m^2/s)	2.36×10^{-5}
a (J.m^3/mol^2)	9.97×10^{-1}
b (m^3/mol)	1.56×10^{-5}
κ (J.m^5/mol^2)	$9.23\times10^{-21}\times(\Delta x/0.012\text{nm})^2$

Table 2. Estimated model parameters for the hydrophilic silicon nanoporous medium

k (m^2)	8.73×10^{-21}
A_h (J/mol)	-2.36×10^{4}
α (m^3/mol)	3.81×10^{-5}
$D_{(g)}$ (m^2/s)	2.78×10^{-7}
$D_{(l)}$ (m^2/s)	3.90×10^{-11}

Figure Captions

Figure 1. Conceptual diagram representing the experimental observation of adsorption and condensation-induced imbibition. Water vapor diffuses into a nanoporous medium under controlled relative humidity and temperature conditions. At high relative humidity conditions, the condensation near the inlet leads to imbibition-type water concentration or saturation profiles.

Figure 2. Comparisons of the model estimated and the measured water concentration profiles at rh=0.98.

Figure 3. Contributions of the diffusive and advective terms to the flux of water as a function concentration.

Figure 4. Dimensionless concentration profiles at a) rh=0.5 ($<rh_{crit}$) and b) rh=0.8($>rh_{crit}$).

Figure 5. The model estimated times for diffusion-to-imbibition transition at 0.68 mm distance from the inlet.

Figure 6. (a) The calculated grand potential energy density (J/m^3) as a function of the normalized water concentration for water-silicon nanoporous medium at various rh. (b) The grand potential diagram representing free energy changes at different rh conditions and different energy barriers for adsorption and desorption.

Figure 7. The model estimated hysteresis in adsorption and desorption isotherms.

Figure A1. Comparisons of the calculated saturated density values using Fuller's equation of state (1976) and the IAPWS formulation for water (Wagner and Pruss, 2002) at different temperatures.

Figure B1. Estimation of the surface tension of water using the square gradient theory-based model. The surface tension data is based on the International Association for the Properties of Water Steam (1994).

Figure B2. Estimated water concentration profiles for a planar interface between liquid and vapor water, using the square gradient theory-based model. $(\kappa/a)^{1/2}$ is roughly equivalent to a molecular diameter. At 15 ^{o}C, the interface thickness is only a few molecular diameters. As the temperature increases, the interface thickness increases, and at a critical temperature, the interface becomes flat and surface tension vanishes.

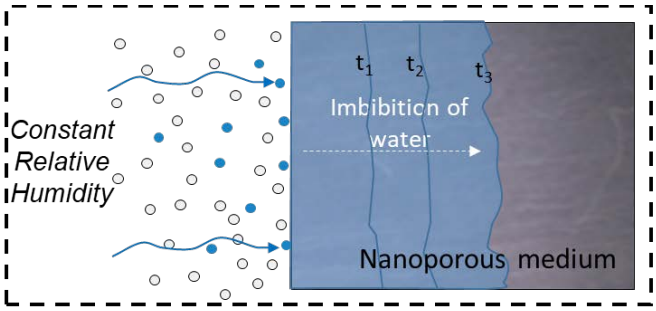

Transition from adsorbed film to pore-filling liquid

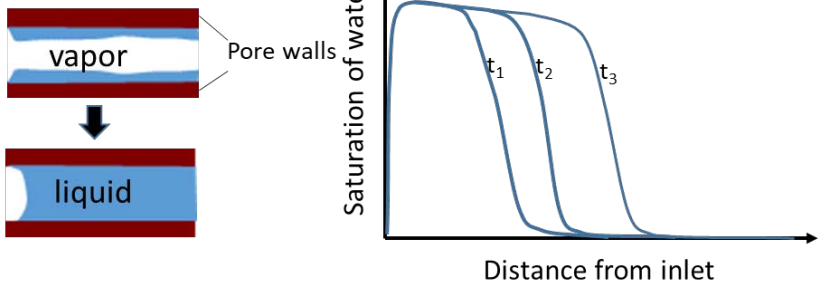

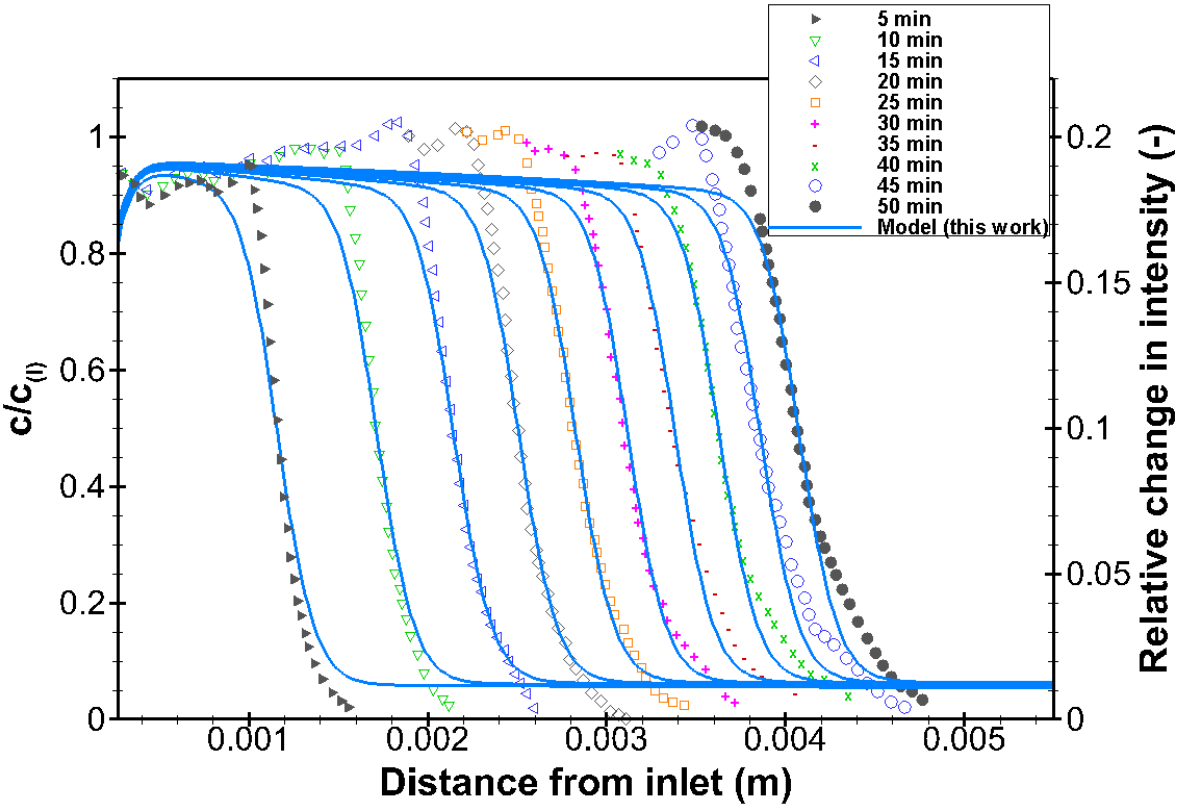
5 min
10 min
15 min
20 min
25 min
30 min
35 min
40 min
45 min
50 min
Model (this work)
c/c(l)
Relative change in intensity (-)
Distance from inlet (m)
0
0.2
0.4
0.6
0.8
1
0.05
0.1
0.15
0.2
0.001
0.002
0.003
0.004
0.005

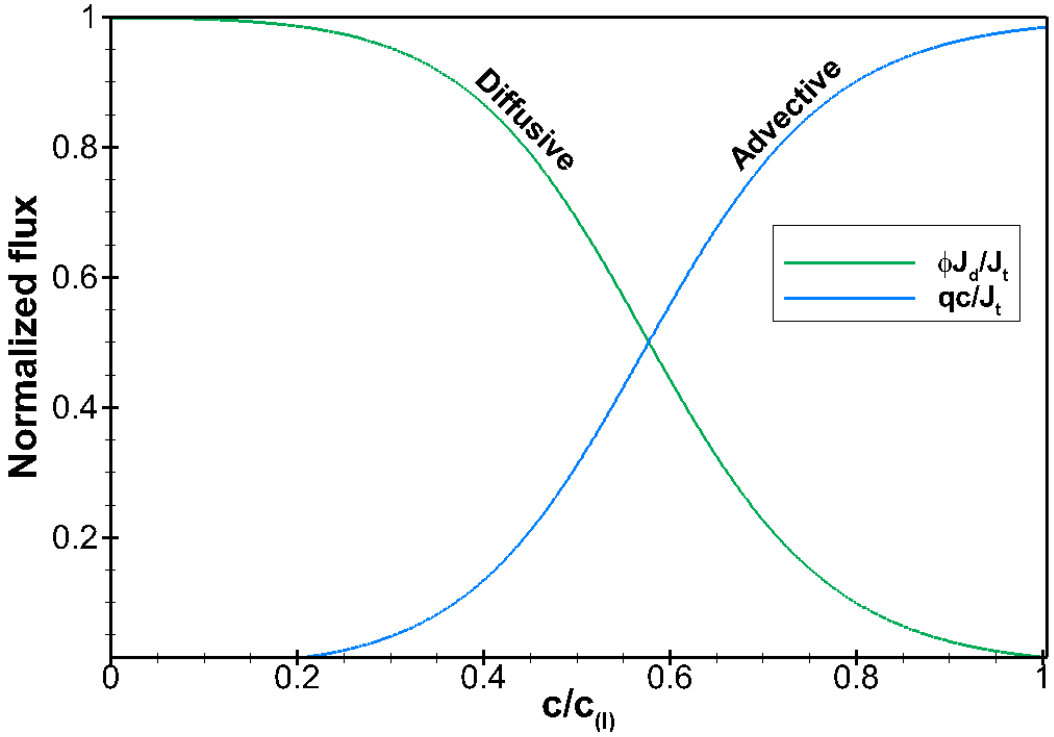
Normalized flux
1
0.8
0.6
0.4
0.2
0
0.2
0.4
0.6
0.8
1
c/c(l)
Diffusive
Advective
ϕJd/Jt
qc/Jt

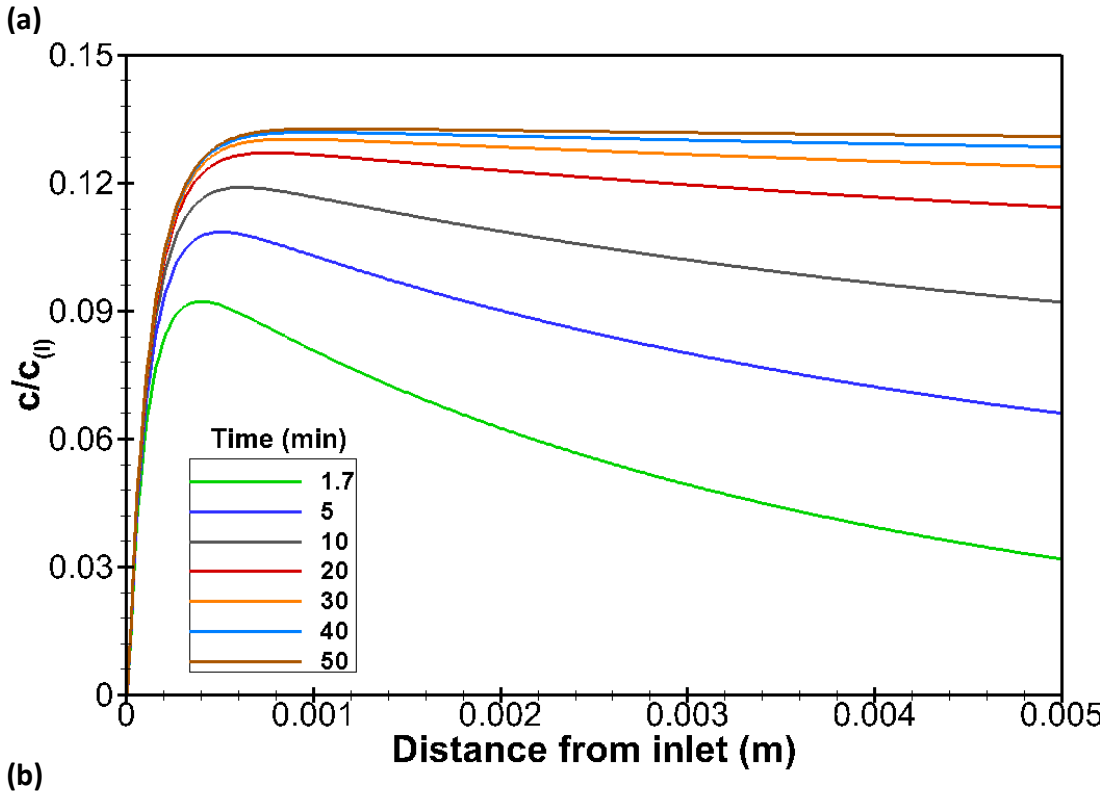
(a)
0.15
0.12
0.09
0.06
0.03
0
c/c(l)
Time (min)
1.7
5
10
20
30
40
50
0
0.001
0.002
0.003
0.004
0.005
Distance from inlet (m)

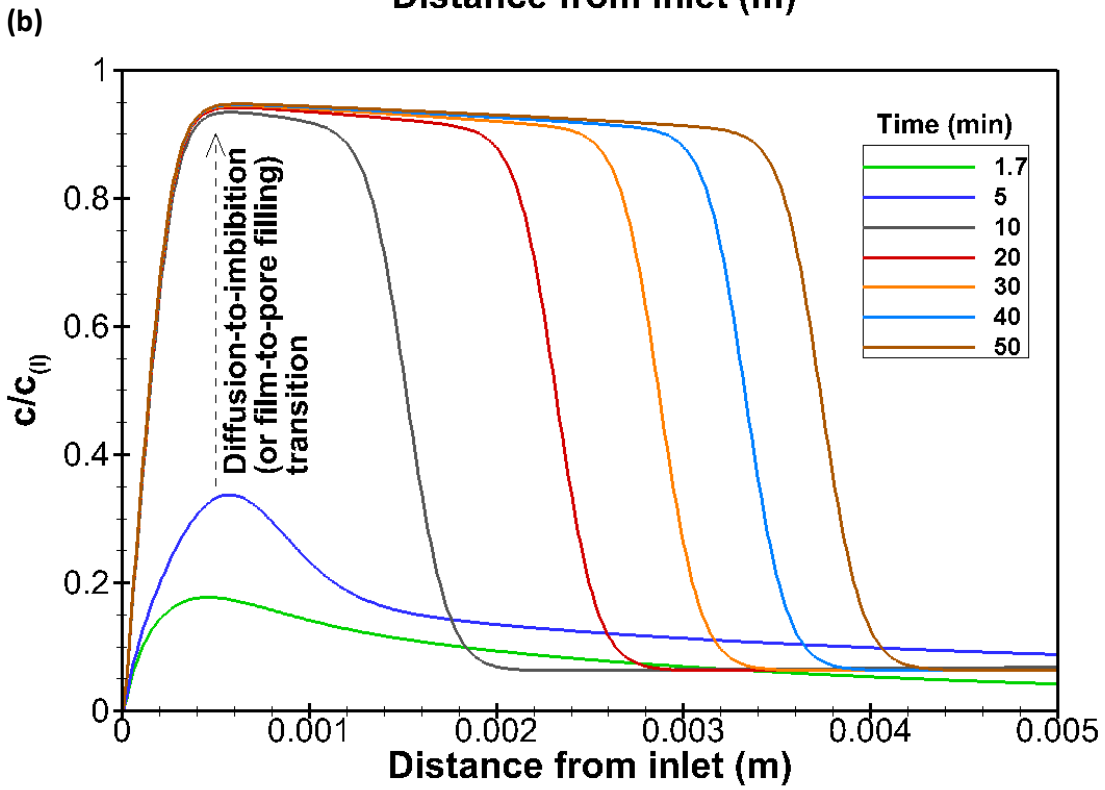
(b)
1
0.8
0.6
0.4
0.2
0
c/c(l)
Diffusion-to-imbibition
(or film-to-pore filling)
transition
Time (min)
1.7
5
10
20
30
40
50
0
0.001
0.002
0.003
0.004
0.005
Distance from inlet (m)

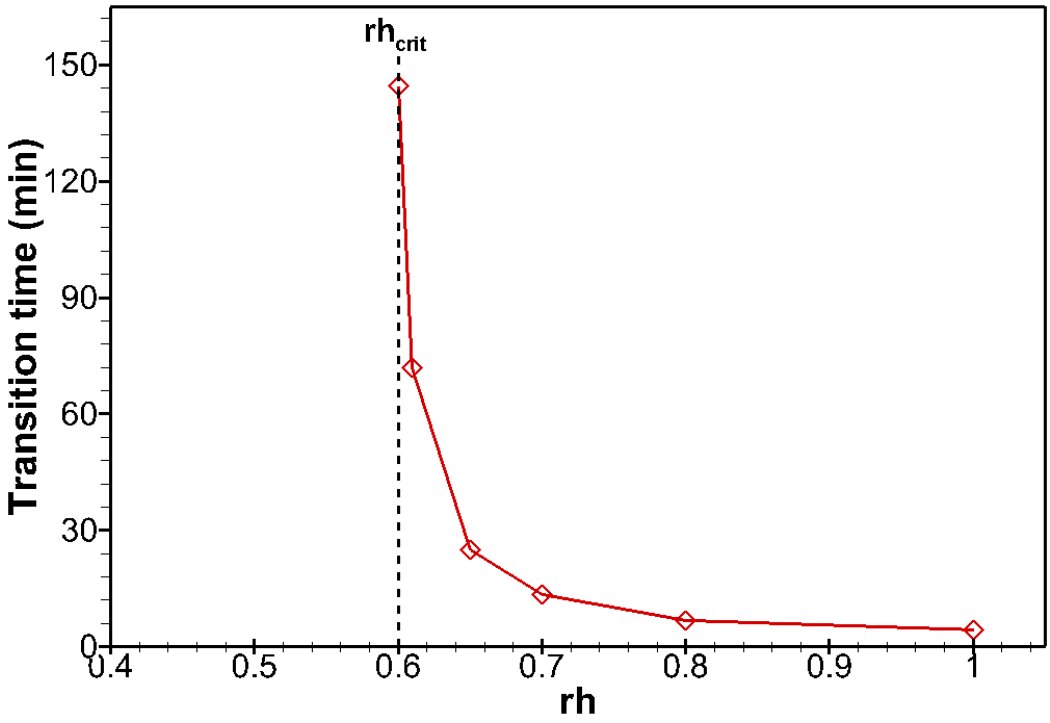
rh_crit
150
120
90
60
30
0
Transition time (min)
0.4
0.5
0.6
0.7
0.8
0.9
1
rh

(a)

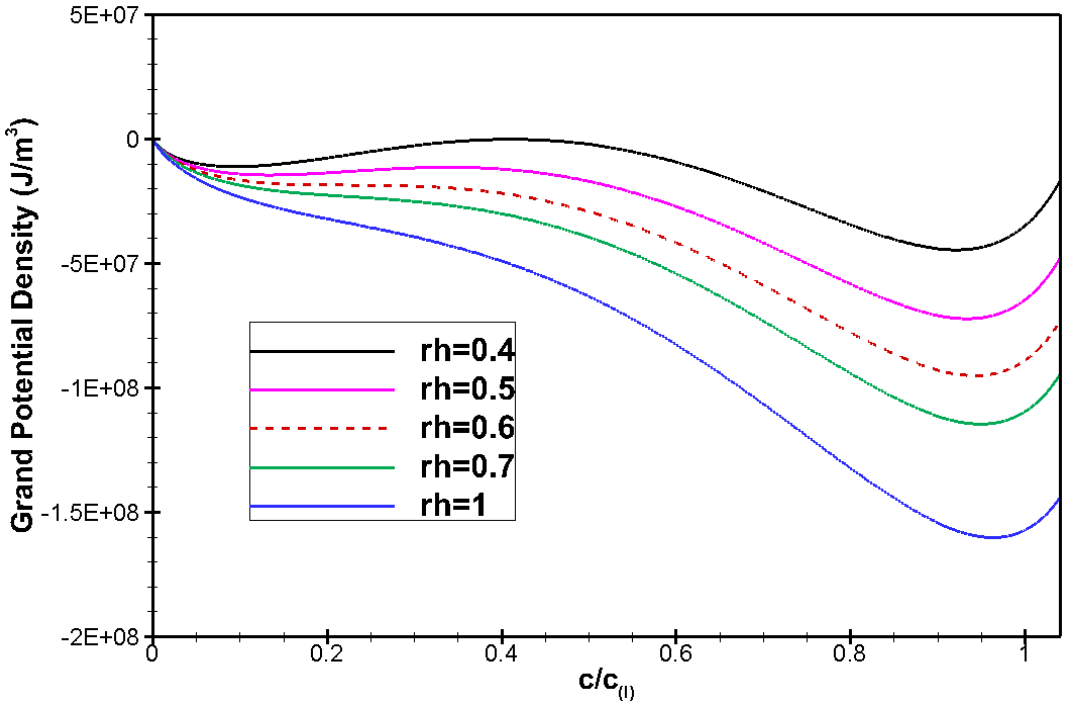
5E+07
0
-5E+07
-1E+08
-1.5E+08
-2E+08
Grand Potential Density (J/m3)
0
0.2
0.4
0.6
0.8
1
c/c(l)
rh=0.4
rh=0.5
rh=0.6
rh=0.7
rh=1

(b)

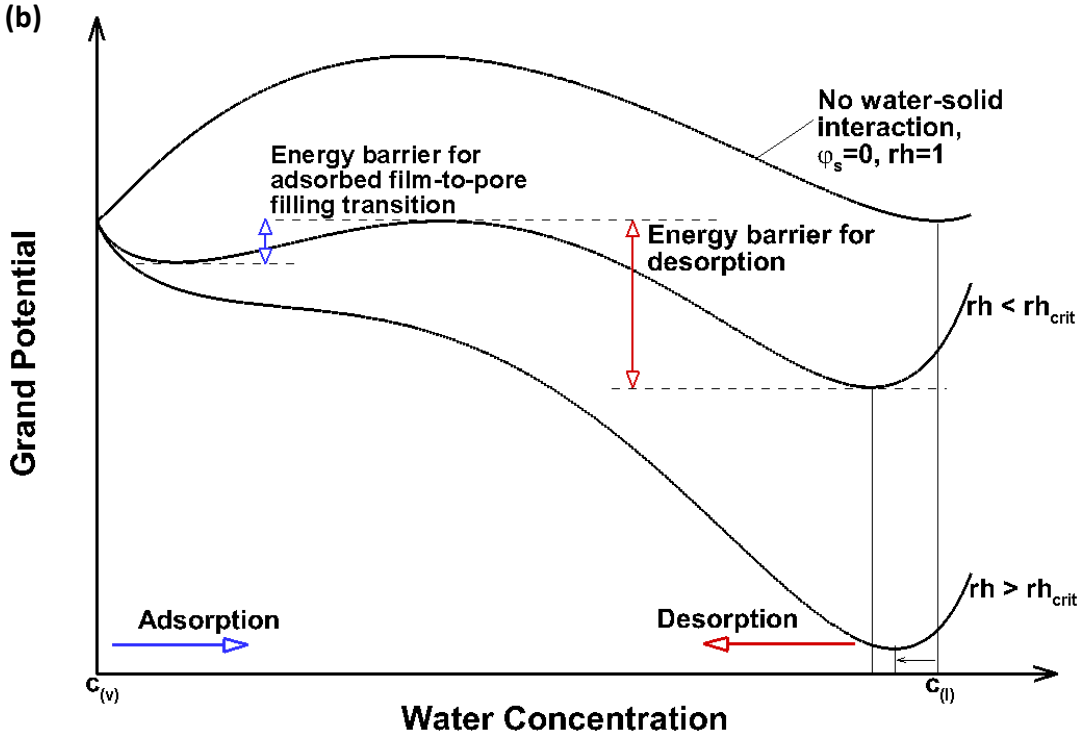
Grand Potential
No water-solid interaction, φs=0, rh=1
Energy barrier for adsorbed film-to-pore filling transition
Energy barrier for desorption
rh < rhcrit
rh > rhcrit
Adsorption
Desorption
c(v)
c(l)
Water Concentration

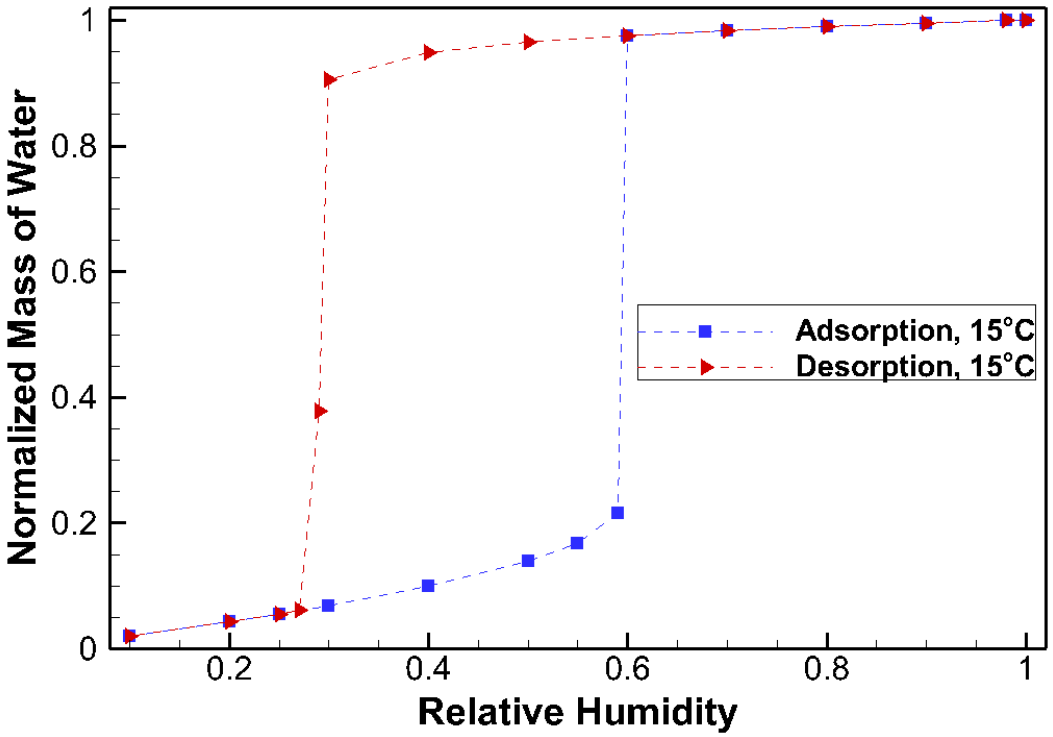
Normalized Mass of Water
Relative Humidity
0
0.2
0.4
0.6
0.8
1
Adsorption, 15°C
Desorption, 15°C

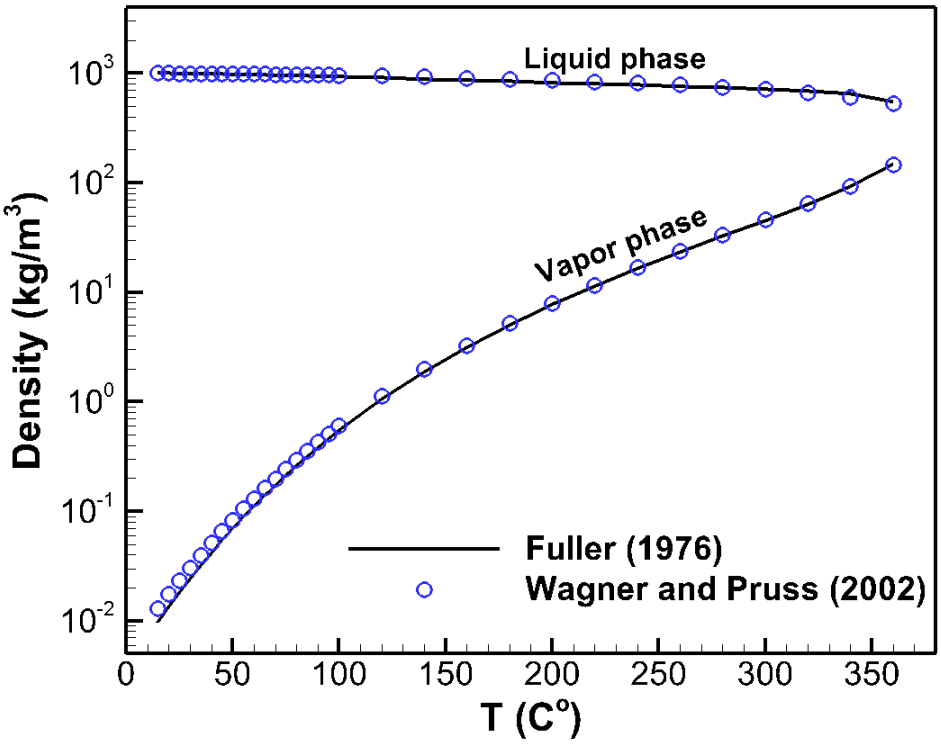
Liquid phase
Vapor phase
Fuller (1976)
Wagner and Pruss (2002)
Density (kg/m^3)
T (C°)
10^3
10^2
10^1
10^0
10^{-1}
10^{-2}
0
50
100
150
200
250
300
350

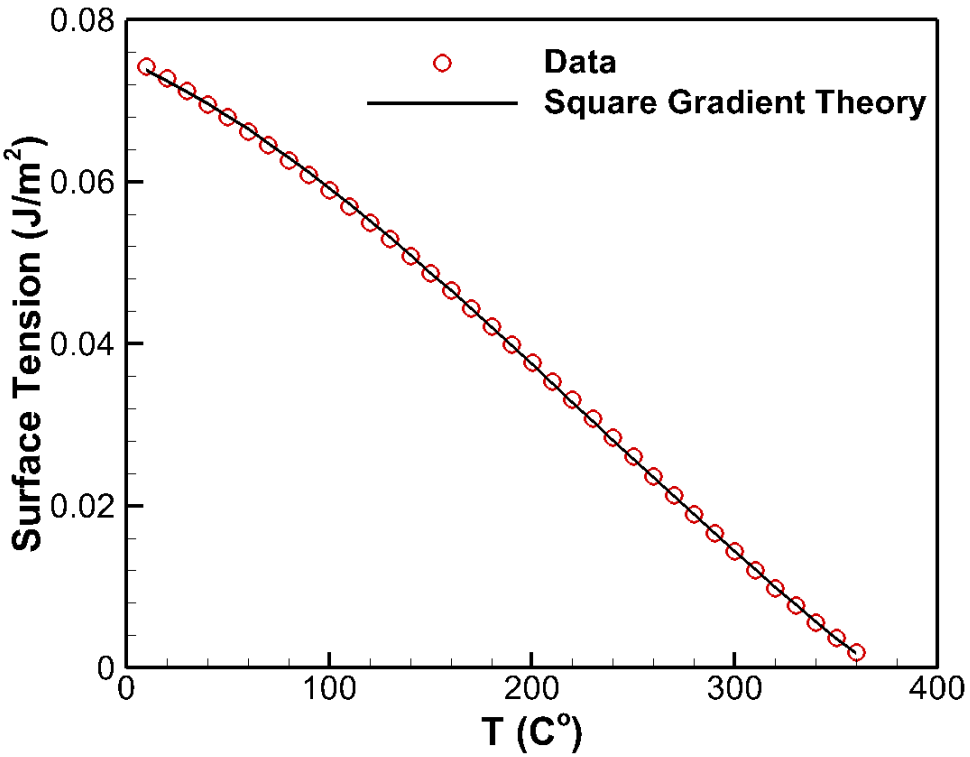
Data
Square Gradient Theory
Surface Tension (J/m^2)
T (C°)
0.08
0.06
0.04
0.02
0
0
100
200
300
400

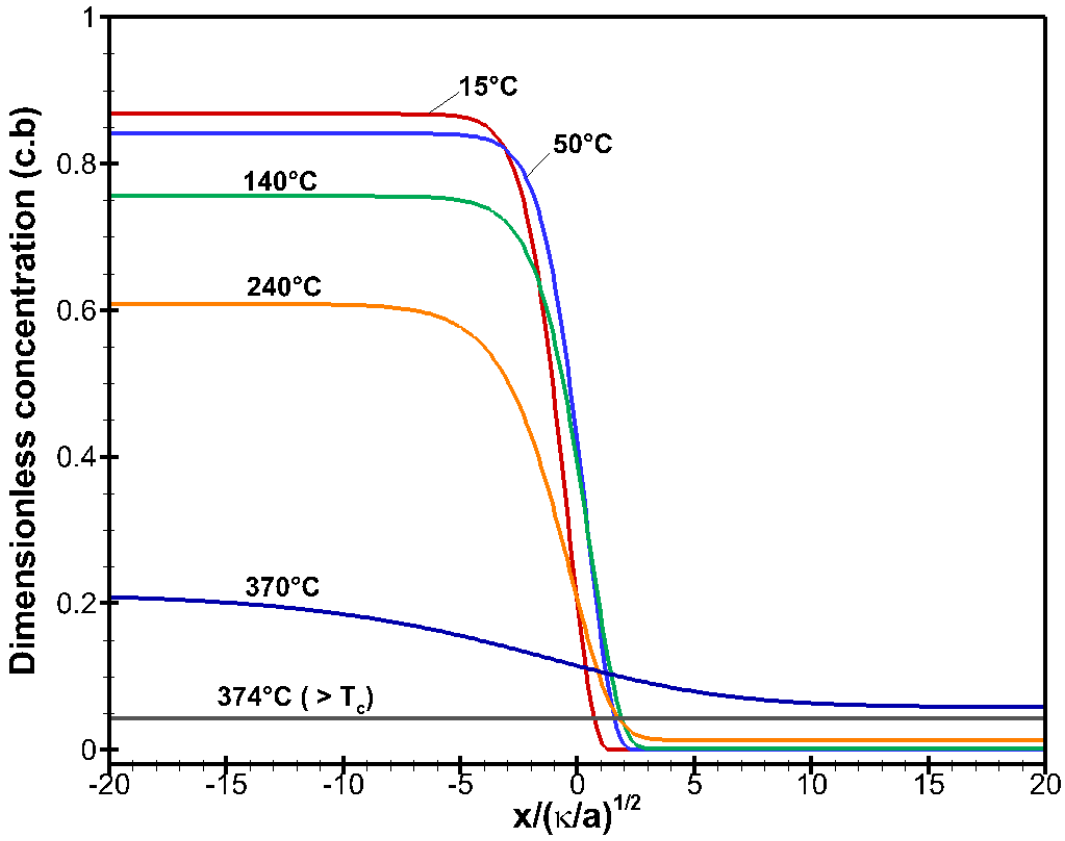
Dimensionless concentration (c.b)
x/(κ/a)^1/2
15°C
50°C
140°C
240°C
370°C
374°C (> T_c)
1
0.8
0.6
0.4
0.2
0
-20
-15
-10
-5
0
5
10
15
20